Time-Dependent Coastal Upwelling[1]

J. DANA THOMPSON AND JAMES J. O'BRIEN

Depts. of Meteorology and Oceanography, and the Geophysical Fluid Dynamics Institute, Florida State University, Tallahassee 32306

(Manuscript received 24 December 1971, in revised form 31 July 1972)

ABSTRACT

Linear and nonlinear two-layer ocean circulation models of coastal upwelling on an f-plane are driven by time-dependent winds and solved numerically. Longshore variations in the circulation are neglected and offshore variations in the winds are specified. A technique for generating a realistic broad frequency-band wind stress from a kinetic energy spectrum of wind speed is developed.

When results from the two models are compared, nonlinearities are found to be unimportant in explaining the basic upwelling dynamics. However, they do provide a mechanism for wave-wave interactions which broaden all spectral peaks. In the nonlinear model coherence-squared spectra between the winds and zonal current components in the upwelling zone indicate highest coherence at lowest frequencies for both layers, accompanied by a 180° phase shift from upper to lower layer at frequencies <3 cycles per day. Similar analyses for winds vs meridional current components and winds vs pycnocline height anomalies show a coherence-squared maximum for winds of 5-day period. In the frequency band below and including the inertial, remarkable similarities are observed between the results of the nonlinear model and actual ocean current autospectra.

1. Introduction

Coastal upwelling off the west coasts of continents affects both the marine ecology and the climate of the adjacent land. The disproportionately high biological productivity in the narrow band of cold upwelled water is economically significant. The reader is referred to Smith (1968) for a complete review of the classical physical processes associated with coastal upwelling.

This paper examines both the linear and nonlinear response of a two-dimensional numerical model of coastal upwelling to a time-dependent wind stress. The two-layer, viscous, f-plane numerical ocean model developed by O'Brien and Hurlburt (1972) is modified for this study. Spatial variations of the winds are included. A technique for generating a realistic, broad frequency-band forcing function from a kinetic energy spectrum of wind speed is developed to provide a temporal realization of the wind stress. Numerical solutions for an irregular bottom similar to the shelf off Pisco, Peru, are discussed.

Current autospectra and coherence-squared spectra between wind speeds and ocean currents are calculated. Nonlinearities are shown to play a minor role in upwelling dynamics, since they only slightly enhance the longshore jet. However, by providing a mechanism for wave-wave interactions the nonlinearities modify the current autospectra by broadening all spectral peaks (such as the inertial). A comparison of the model with actual oceanic spectra reveals remarkable similarity in the frequency band below and including the inertial.

[1] Contribution No. 73 of the Geophysical Fluid Dynamics Institute, Florida State University, Tallahassee.

2. The two-layer model

The following discussion, after O'Brien and Hurlburt (1972), briefly describes the formulation of a two-layered, two-dimensional ocean with bottom topography. For a complete discussion of the n-layered ocean problem, their article should be consulted.

Consider a two-layered ocean on an f-plane with all longshore variations neglected. The coordinate system is Cartesian with z increasing upward and x increasing eastward (Fig. 1). The governing equations are

$$\frac{\partial u_1}{\partial t}+u_1\frac{\partial u_1}{\partial x}+g\frac{\partial}{\partial x}(h_1+h_2+D) = fv_1+(\tau_{Sx}-\tau_{Ix})/(\rho h_1)+A\frac{\partial^2 u_1}{\partial x^2}, \quad (1)$$

$$\frac{\partial v_1}{\partial t}+u_1\frac{\partial v_1}{\partial x} = -fu_1+(\tau_{Sy}-\tau_{Iy})/(\rho h_1)+A\frac{\partial^2 v_1}{\partial x^2}, \quad (2)$$

$$\frac{\partial h_1}{\partial t}+\frac{\partial (h_1u_1)}{\partial x}=0, \quad (3)$$

$$\frac{\partial u_2}{\partial t}+u_2\frac{\partial u_2}{\partial x}+g\frac{\partial}{\partial x}(h_1+h_2+D)-g'\frac{\partial h_1}{\partial x} = fv_2+(\tau_{Ix}-\tau_{Bx})/(\rho h_2)+A\frac{\partial^2 u_2}{\partial x^2}, \quad (4)$$

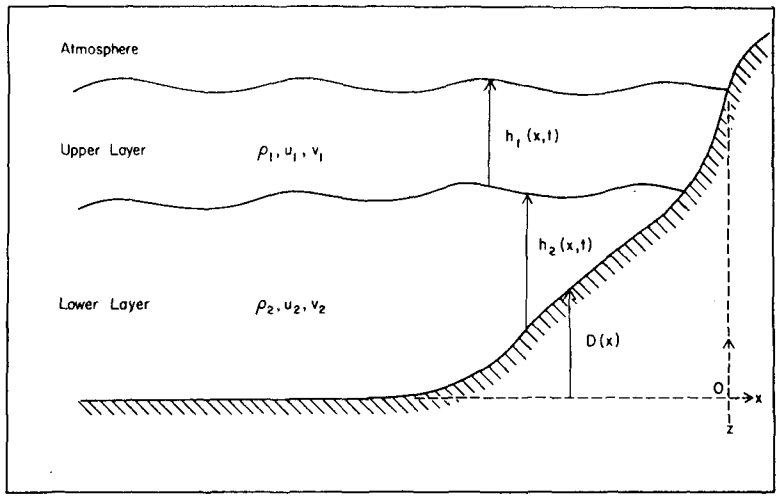

FIG. 1. Typical geometry for a two-layer model with a free surface and one interface. The bottom topography is $D(x)$; h_1 and h_2 are the thicknesses of each layer of density ρ_1 and ρ_2. The velocities are depth-averaged.

$$\frac{\partial v_2}{\partial t}+u_2\frac{\partial v_2}{\partial x}=-fu_2+(\tau_{Iy}-\tau_{By})/(\rho h_2)+A\frac{\partial^2 v_2}{\partial x^2}, \tag{5}$$

$$\frac{\partial h_2}{\partial t}+\frac{\partial (h_2u_2)}{\partial x}=0, \tag{6}$$

where:

$$\left.\begin{aligned} g'&=g(\rho_2-\rho_1)/\rho_2\\ \tau_{Ix}&=\rho C_I\bar{q}(u_1-u_2)\\ \tau_{Iy}&=\rho C_I\bar{q}(v_1-v_2)\\ \tau_{Bx}&=\rho C_Bq_2u_2,\quad \tau_{By}=\rho C_Bq_2v_2\\ q_i&=(u_i^2+v_i^2)^{\frac{1}{2}}\\ \bar{q}&=(q_1+q_2)/2 \end{aligned}\right\}. \tag{7}$$

The subscript 1 refers to the upper layer and 2 to the lower layer. The onshore and longshore velocity components, u_i and v_i, respectively, are instantaneous and depth-averaged. The first subscript in the stress terms τ refers to the surface (S), the interface (I), or the bottom (B). Instantaneous thicknesses of the upper and lower layers are h_1 and h_2, respectively. $D(x)$ is the height of the bottom topography above some reference level. The pressure is hydrostatic.

Eqs. (1)–(6) represents six nonlinear, time-dependent equations in six unknowns: u_1, u_2, v_1, v_2, h_1, h_2. At the coast $u_1=v_1=u_2=v_2=0$, and h_1 and h_2 are determined from the continuity equation using a one-sided difference. The far-wall boundary conditions are also no-slip and kinematic. More properly, a radiational condition or the method of characteristics should be used there, although for a reasonably wide channel (>300 km), the inshore solutions are little affected by the open ocean boundary conditions.

The variables $D(x)$, f, A and the surface wind stress are specified. In the present case $f=10^{-4}$ sec^{-1}, $A=10^6$ cm^2 sec^{-1}, and the topography is shown in Fig. 2. Note that attention is confined to the case in which the free surface and the interface intersect a vertical boundary at the coast, in contrast to the sloping boundary problem considered by Sielecki and Wurtele (1970). Suppose that shoreward of 100 km there exists a shallow shelf at depth 64 m. Over the shelf the lower layer is 14 m thick initially, whereas seaward of 100 km it is 150 m thick initially. The density discontinuity at 50 m is a simple representation of the pycnocline.

O'Brien and Hurlburt (1972) specify equal interfacial and bottom stress constants ($C_I=C_B=3\times10^{-4}$). Even when a larger, more realistic value for C_B is used, we find bottom friction to be relatively unimportant as shown by Johnson (1970). We have chosen $C_B=1\times10^{-3}$ after Bye (1970) and Proudman (1953). The interfacial stress constant is estimated from the following scaling argument.

Assume that momentum transfer between layers in this model due to vertical current shear is equivalent to the transfer of momentum due to vertical eddy diffusion in a continuously stratified model, i.e.,

$$\frac{\tau_{Iy}}{\rho h_1}=\frac{\partial}{\partial z}\left(A_v\frac{\partial v}{\partial z}\right). \tag{8}$$

If H is the scale depth and V the velocity scale, Eq. (8) and the definition of τ_{Iy} yield

$$C_I\approx\frac{A_v}{HV}. \tag{9}$$

Kullenberg (1971) has shown that the vertical eddy viscosity in shallow water is related to the Richardson number and may vary over orders of magnitude. In order to neglect thermohaline mixing, internal consistency in the model requires the vertical transport time

scale to be at least one order of magnitude less than the diffusive time scale. This condition provides the scaling relation $A_v \leqslant 0.1\ HW$, where W is the vertical velocity scale. For $H=5\times10^3$ cm (Table 1) and a typical upwelling vertical velocity of 10^{-3} cm sec^{-1}, this yields $A_v \leqslant 0.5$ cm^2 sec^{-1}. Upon evaluating Eq. (9) we find $C_I \leqslant 1\times10^{-5}$. The upper limit is taken as the model value and it agrees exactly with that used by Pike (1971) for equatorial upwelling.

The quadratic stresses in this model may not be the best formulation. However, since O'Brien and Hurlburt (1972) showed that these do not play an important role in the spin-up of the model, reformulation seems academic. As a reviewer points out, we may assume that Ekman layers exist at the interfaces and the bottom and one may formulate the interfacial and bottom stresses based on Ekman layer dynamics and continuity of stress and velocity across the interface. Perhaps a more serious objection to the present stress formulation is that it is not invariant to a coordinate transformation (D. Caldwell, personal communication). This is corrected if $\bar{q}$ is redefined as

$$\bar{q}=|\hat{\mathbf{q}}_1-\hat{\mathbf{q}}_2|,$$

where $\hat{\mathbf{q}}_i$ is the horizontal velocity vector.

In this paper we will display solutions of a nonlinear model and a quasi-linear model, henceforth referred to as the linear model. In the quasi-linear formulation we have omitted the advective terms from the momentum equations. The stress terms take the form

$$(\tau_{Sy}-\tau_{Iy})/(\rho H_1),$$

where the initial layer thicknesses H_1, H_2 are retained for all time. The stress itself retains a nonlinear character. The lower layer continuity equation allows variation in h_2 due to bottom topography only. Hence, the continuity equations are

$$\left.\begin{aligned}&\frac{\partial h_1}{\partial t}+H_1\frac{\partial u_1}{\partial x}=0\\&\frac{\partial h_2}{\partial t}+\frac{\partial}{\partial x}[H_2(x)u_2]=0\end{aligned}\right\}. \tag{10}$$

Both linear and nonlinear models are solved numerically.

The numerical scheme, patterned after Kwizak and Robert (1971), is semi-implicit, treating the pressure gradient terms, the divergence terms in the continuity equations, and the diffusive terms implicitly. Thus, both external and internal gravity wave modes are treated implicitly. When compared to the purely explicit method, computational efficiency is increased at least eighty-fold with no decrease in accuracy. Leap-frog in time, quadratic averaging for the advective terms (Grammeltvedt, 1969), and centered-in-time for the Coriolis terms complete the numerical framework. A detailed discussion of the numerical procedure may be found in O'Brien and Hurlburt (1972).

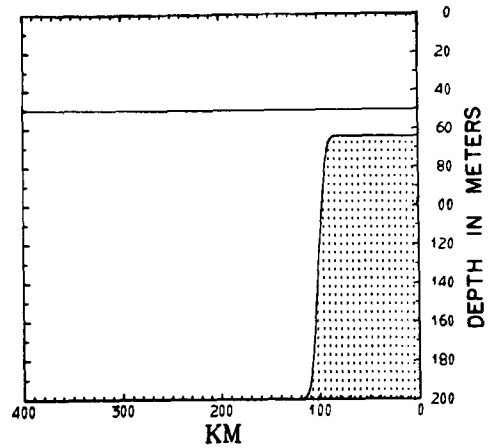

FIG. 2. Geometry for the models. Initially the upper layer is 50 m thick, and the lower layer is 14 m thick near the coast and 150 m thick off shore.

3. A time-dependent forcing

In the numerical modeling of geophysical systems, the application of a realistic forcing function to the governing equations is of critical importance. In coastal upwelling the primary forcing is the surface wind stress, which is strongly time-dependent. Heretofore, however, mainly steady-state dynamical descriptions of the upwelling process have been considered (Hidaka, 1954; Yoshida, 1967). We intend to examine more closely the time-dependent nature of coastal upwelling under variable winds, comparing the single realization from our model with actual observations (e.g., Huyer and Pattulo, 1972; Mooers *et al.*, 1972).

Because little is known about the time and space variations of winds over the upwelling region, proper specifications of the forcing function is difficult. We have sought to realistically formulate the temporal variation of the wind stress while retaining a rather simple spatial distribution of wind stress.

As an alternative to applying actual wind data from an upwelling area directly to the numerical model, we employ a method suggested by Hino and Hino (1965) whereby wind oscillations covering a broad spectral band serve as the model forcing. We assume that over

TABLE 1. Constants of the model and scaling parameters.

Parameter	Value	Parameter	Value
f	10^{-4} sec^{-1}	H	50 m
g	10^3 cm sec^{-2}	V	10 cm sec^{-1}
g'	2 cm sec^{-2}	H_1	5×10^3 cm
A	10^6 cm^2 sec^{-1}	H_2	15×10^3 cm
ρ	1 gm cm^{-3}		
C_I	10^{-5}	Δx	4 km
C_B	10^{-3}	Δt	30 min

the upwelling region kinetic energy spectra of wind speed are identical for every point in the zone. Further, the wind stress does not vanish at the coast, in contrast to Hsueh and Kenney (1972).

a. An explanation of the method

Let $x(t)$ be a realization of a stationary process, composed of N equally-spaced elements x_k, $k=(-n)(1)(n-1)$. [This notation means that k increases from $-n$ to $n-1$ in units of 1]. Total record time is $N\Delta$, where Δ is the sampling interval and N is assumed even, i.e., $N=2n$, where n is an integer. Assume that the power spectrum $H(f)$ for the process is known over a continuous frequency range $f_{\min}$ to $f_{\max}$, where $f_{\min}=1/N\Delta$, $f_{\max}=1/2\Delta$. The limits of the frequency band are thus bounded by the fundamental and Nyquist frequencies of the realization. The spectrum is symmetric and only positive frequencies are considered.

If the stationary process refers to wind speed, then the kinetic energy per unit mass in the frequency band df is

$$S(f)df=H(f)d\ln f, \tag{11}$$

where $S(f)$ is the sample spectrum. A plot of $H(f)$ vs $\ln f$ is commonly called a kinetic energy spectrum for the process.

In terms of discrete frequencies of the realization, $f_m=m/N\Delta$, $m=1(1)n$, and the spectral estimate $S(f_m)$ can be related to the contribution to variance s_m^2 at f_m by

$$S(f_m)=N\Delta\, s_m^2, \tag{12}$$

where

$$s_m^2=\begin{cases}\frac{1}{2}(a_m^2+b_m^2), & m\neq 0, n,\\ \frac{1}{4}a_n^2, & m=n,\end{cases} \tag{13}$$

and a_m and b_m are the Fourier cosine and sine coefficients, respectively.

Using (11) and (12), the contribution to variance at the mth harmonic can be related to the power spectrum by

$$s_m^2=\frac{H(f_m)}{N\Delta f_m}, \quad m=1(1)n. \tag{14}$$

If we assume relations of the form

$$\left.\begin{aligned}a_m^2&=c_m^2 s_m^2\\ b_m^2&=(2-c_m^2)s_m^2\end{aligned}\right\}, \quad m\neq 0, n$$
$$a_n^2=4s_n^2, \tag{15}$$

then the magnitude of the Fourier coefficients are specified to within a multiplicative factor c_m^2. We require $0\leqslant c_m^2\leqslant 2$, and c_m^2 must be specified for each harmonic m, as must the signs of the coefficients a_m and b_m and the mean $a_0/2$. Once these coefficients are determined, a realization x_k is easily generated from the usual expansion

$$x_k=\tfrac{1}{2}a_0+\sum_{m=1}^{n-1}\left(a_m\frac{\cos 2\pi mk}{N}+b_m\frac{\sin 2\pi mk}{N}\right)+\tfrac{1}{2}a_n\cos\frac{2\pi nk}{N}, \tag{16}$$

$k=(-n)(1)(n-1)$.

Thus, from a known kinetic energy spectrum of wind speed in the frequency domain we can generate a realization of wind speeds in the time domain. The realization depends on the Fourier coefficients a_m and b_m and hence on our selection of c_m^2. It is important to note, however, that each realization we obtain through arbitrary choice of the c_m^2 has the same distribution of kinetic energy over frequency. The generated data ensemble maintains in real space all of the original information contained in the frequency domain and represented by the sample spectrum.

b. The wind generator

Millard (1971) has presented a composite kinetic energy spectrum of wind speed over the sea for periods from 20 days to 2 sec. Fig. 3 shows the smooth line as an analytic approximation to the Millard spectrum with exclusion of high frequencies [>1 cycle per hour (cph)] and extension of the low frequency end to 25 days. This analytical function is assumed to be the "true" kinetic energy spectrum for wind speed adjacent to an eastern ocean boundary.

The ordinate of Fig. 3, $H(f_m)$, is the product of frequency and corresponding spectral estimate $S(f_m)$. Multiplying by a power transfer function $\zeta(f_m)$ at discrete frequencies, the "true" kinetic energy spectrum is transformed into the jagged line of the figure, the realization spectrum.

The power transfer function $\zeta(f_m)$ is defined as

$$\zeta(f_m)=1+R(f_m), \tag{17}$$

where $R(f_m)$ is a random white noise variable with range -0.2 to $+0.2$. Consequently, $\zeta(f_m)$ varies in a random manner from 0.8 to 1.2. The power transfer function effectively introduces a degree of variability into the spectrum, similar to what one would observe in a natural stochastic realization. The choice of the range of $R(f_m)$ was quite arbitrary and no deep significance would be attached to it.

Once the realization spectrum is obtained, Eqs. (14) and (15) are employed to calculate contributions to variance s_m^2 at each harmonic. For our problem, the value of c_m^2 was then randomly partitioned between 0 and 2 and the sign of a_m and b_m likewise randomly assigned. Next, the transformation from the frequency domain to the time domain was accomplished by application of the fast Fourier transform. Fig. 4 shows the

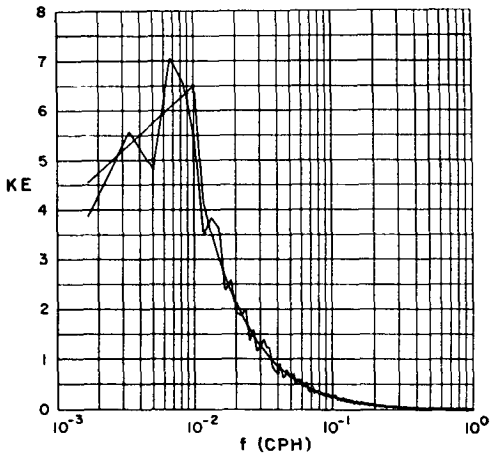

FIG. 3. The kinetic energy of wind speed over the ocean ($m^2 sec^{-2}$) vs frequency (cph), due to Millard (1971). The smooth line is the analytic approximation to the observed spectrum and the jagged line is the realization.

generated winds at 30-min intervals with mean wind speed set to zero. In a real coastal upwelling situation the mean wind would be equatorward. Note that this sequence of winds has a nearly Gaussian distribution.

We have employed Millard's (1971) kinetic energy spectrum of wind speed as the spectrum of longshore winds only. This procedure is valid for two reasons. First, coastal upwelling can be shown to have very weak dependence on onshore wind stress. Second, during the upwelling season the winds are generally observed to be primarily longshore (Pillsbury, 1972).

The value of the stress at a given point and time is obtained from

$$\left.\begin{aligned}\tau_{Sy}(x,t) &= -W(x)[\tau_{Sy}'(t)]\\ \tau_{Sx} &= 0\end{aligned}\right\}, \qquad (18)$$

in which

$$\tau_{Sy}'(t) = C_D \rho_a |V_a| V_a,$$

where V_a is the longshore wind speed, ρ_a the density of the air, and C_D the drag coefficient. The product $\rho_a C_D$ was chosen such that the maximum τ_{Sy}' is 3 dyn cm^{-2}. This implies a C_D of order 10^{-3}. The spatial weighting function $W(x)$ is shown in Fig. 5. The stress is independent of x for $x \epsilon [0, -200\text{ km}]$ and drops off rapidly in magnitude 200 km off the coast.

4. Results

The linear and nonlinear versions of the numerical model were driven by the generated wind stress for a period of 25 days, starting from rest. Instantaneous profiles of velocity and deviations of the free surface and interfacial heights in time and space are presented. Coherence-squared spectra and phase diagrams for currents are shown and current autospectra from the nonlinear model and from observations are compared.

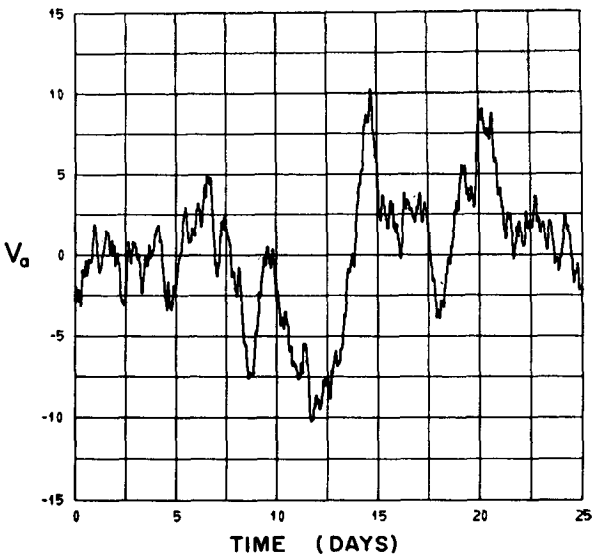

FIG. 4. Longshore winds (m sec^{-1}) vs time (days). Negative values indicate northerly winds.

a. *Instantaneous profiles*

Fig. 6 provides a direct comparison between current profiles for the linear and nonlinear models at day 12. Fig. 7 shows deviations of interfacial and free surface height from the initial values. A height anomaly which is decreasing (increasing) with time corresponds to downwelling (upwelling).

Fig. 6 indicates nearly identical results for both the linear and nonlinear models. Equatorward flow from near the coast in both layers results from the strong northerly winds that persist from day 10. This period includes the onset of significant upwelling. The coastal jet found in the upper layer ~8 km offshore has dynamics similar to those discussed by Charney (1955) for the Gulf Stream and is a baroclinic extension of the classical Ekman (1905) description of upwelling dy-

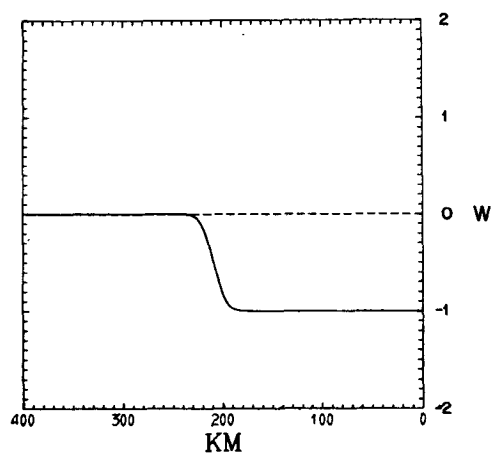

FIG. 5. Value of the wind stress weighting function W vs distance offshore.

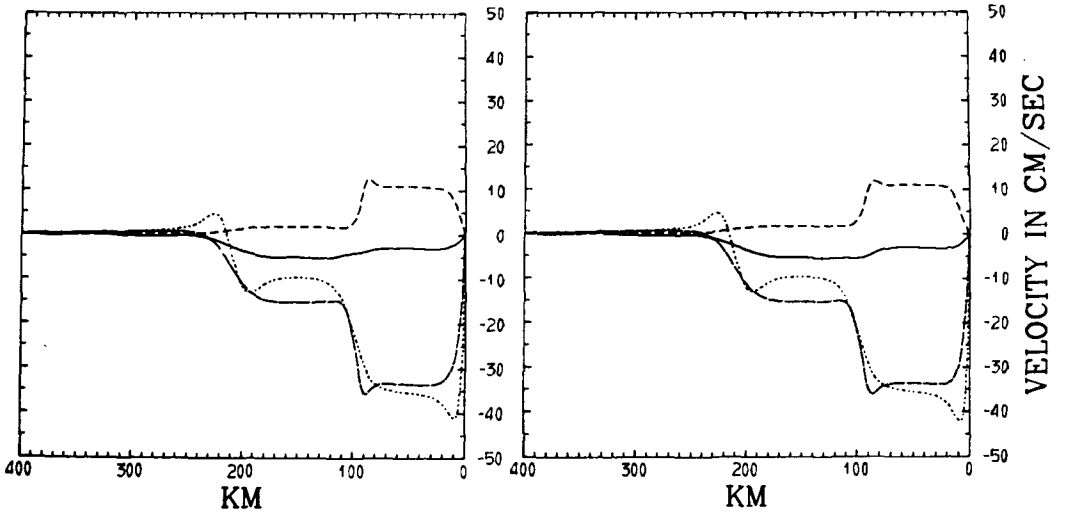

FIG. 6. Velocity profiles vs x for the linear (left) and nonlinear (right) models at day 12. Line representations are solid (u_1), small dashes (v_1), medium dashes (u_2), long dashes (v_2).

namics. The jet exists solely as a time-dependent phenomenon and cannot be described by the steady-state equations (O'Brien and Hurlburt, 1972).

The slight enhancement of the longshore jet in the nonlinear model is due to the decrease of h_1 near the coast, increasing the magnitude of the surface stress term, i.e., the forcing function. In contrast, the linear model requires h_1 to remain at its initial state value. The lower layer longshore jet just inshore of the shallow shelf is a highly transient feature, appearing only during major reversals of the wind.

From mass conservation we find, for slowly changing conditions,

$$u_2 h_2 \approx -u_1 h_1,$$

which requires that onshore flow in the lower layer be compensated by offshore flow in the upper layer. This simple compensation relation implies that over the shallow shelf $|u_2| > |u_1|$. Fig. 6 verifies this result.

Fig. 7 depicts two zones of active upwelling. The primary zone at the coast is roughly 30 km wide and the interfacial height anomaly reaches a maximum of 14 m at the coastal boundary. The secondary upwelling zone occurs over the shelf break with the same width scale (30 km) as the sloping shelf edge. Increasing the bottom slope increases the maximum height anomaly of the secondary upwelling zone and decreases its width. Secondary upwelling is a transient feature which disappears under a steady wind stress. It has been observed by Bang (1971) off the west coast of Africa in the southern Benguela Current. For small values of interfacial and bottom stress the maximum secondary up-

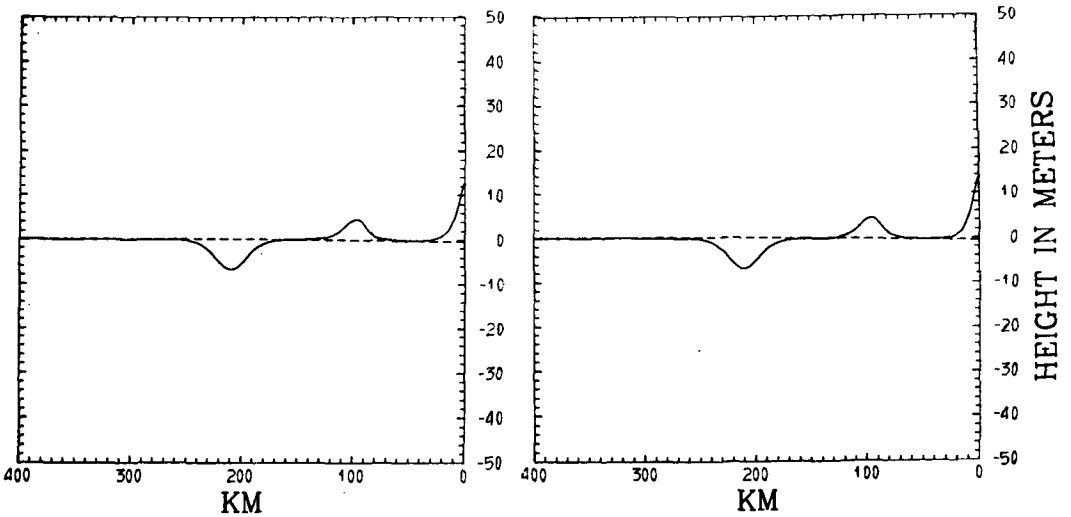

FIG. 7. Height anomalies for the linear (left) and nonlinear (right) models at day 12. The dashed line is the free surface height anomaly and the solid line the interfacial height anomaly.

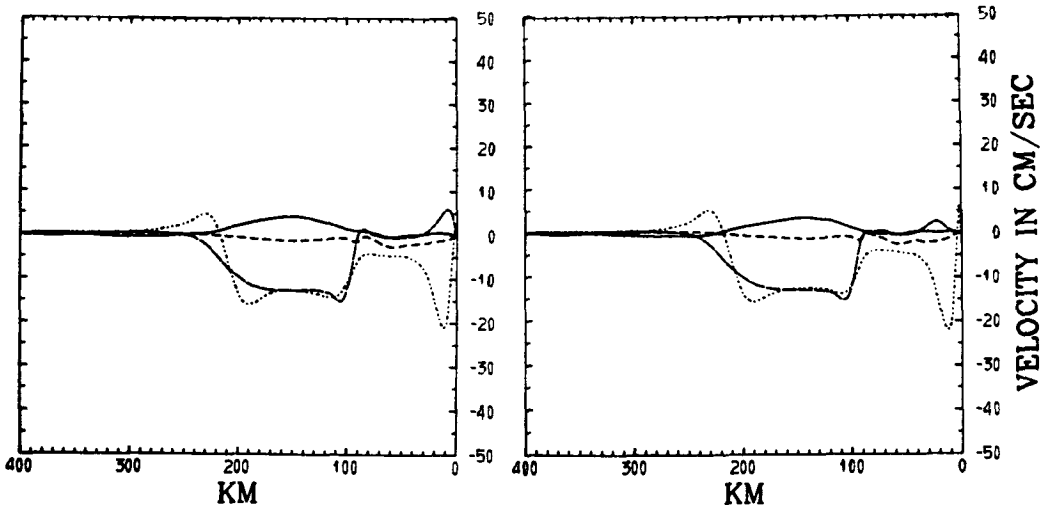

FIG. 8. Velocity profiles for the linear (left) and nonlinear (right) models at day 15. Line representations are as in Fig. 6.

welling height anomaly equals that at the coastal boundary. Alternatively, Hsueh and O'Brien (1971) explain secondary upwelling in terms of large-scale currents.

Following O'Brien and Hurlburt (1972) both the primary and secondary upwelling can be explained in terms of a potential vorticity argument, which asserts that

$$\frac{\partial v_1}{\partial x}=f\left(\frac{h_1-H_1}{H_1}\right), \tag{19}$$

$$\frac{\partial v_2}{\partial x}=f\left(\frac{h_2-H_2}{H_2}\right), \tag{20}$$

where H_1 and H_2 are initial thicknesses for the two layers. At the shelf edge, v_1 decreases shoreward under northerly winds, hence $h_1<H_1$ and upwelling is observed. Similarly, near the coast, the equatorward jet in v_1 is associated with upwelling.

Broad downwelling located 200 km from the coast is a result of Ekman pumping. Sufficiently far offshore Eq. (2) reduces to the Ekman relation

$$u_1h_1=\tau_{Sy}/(\rho f). \tag{21}$$

Combining this with (3), we obtain

$$\frac{\partial h_1}{\partial t}=-\frac{\partial(\tau_{Sy}/\rho f)}{\partial x}. \tag{22}$$

Negative curl in the wind stress produces increasing h_1 or downwelling. Although downwelling is dependent on the wind stress curl, the upwelling at the coast depends on wind stress.

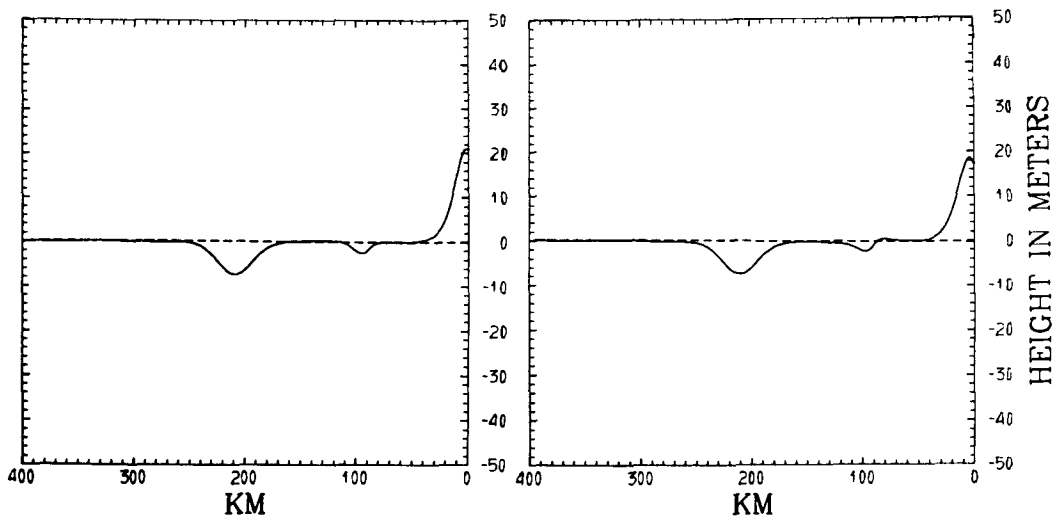

FIG. 9. Height anomalies for the linear (left) and nonlinear (right) models at day 15. Line representations are as in Fig. 7.

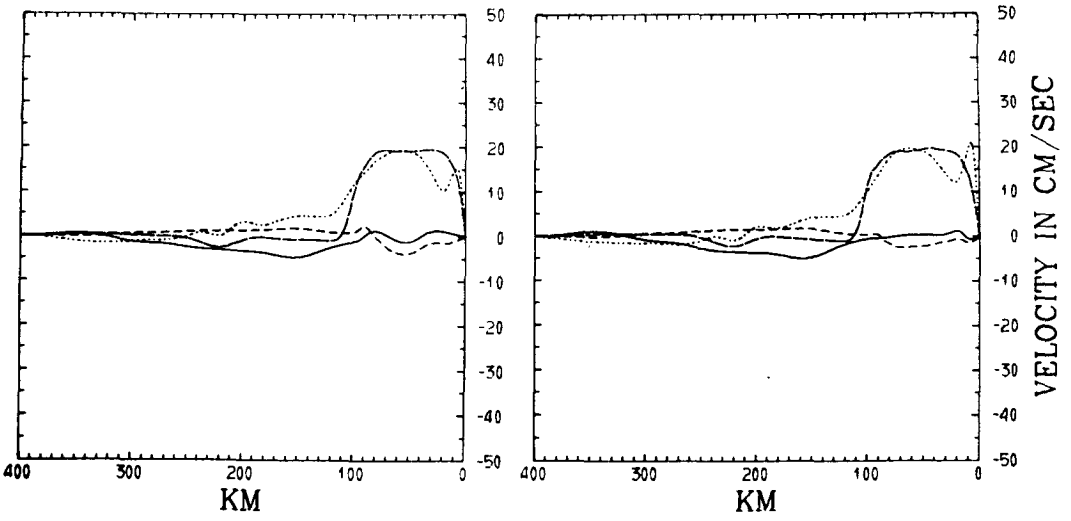

FIG. 10. Velocity profiles for the linear (left) and nonlinear (right) models at day 22. Line representations are as in Fig. 6.

The pronounced shift to southerly winds at day 13 suggests the need for a second "snapshot" of velocities and height anomalies. Fig. 8 depicts the instantaneous velocity profiles for both models at day 15, and Fig. 9 shows the height anomalies at the same time.

The velocity profiles show considerable weakening of the equatorward flow in the upper layer, as is expected under strong southerly winds. The longshore jet, while still defined, has decreased from its maximum of -55 cm sec^{-1} at day 13 to -20 cm sec^{-1}. A poleward jet has developed in the lower layer within 20 km of the coast. The jet is less intense in the nonlinear model. Furthermore, the position of the jet maximum has been shifted from 10 km offshore in the linear model to 20 km offshore in the nonlinear case.

To explain these features consider geostrophic balance in the longshore velocities for both layers. The baroclinic component of longshore velocity is

$$f(v_1-v_2)=g'\frac{\partial h_1}{\partial x}. \tag{23}$$

Referring to Fig. 9 we find that $\partial h_1/\partial x$ is a negative constant from 20 to 5 km off shore in the linear model. According to Eq. (23), the maximum in v_2 within this zone must occur where v_1 is a minimum. This is observed in the model. In contrast, the nonlinear model includes advection, which tends to transport the lower layer poleward jet off shore.

Fig. 10 depicts the velocity profiles at day 22 and Fig. 11 shows the height anomalies at the same time for both models. Winds have blown southerly three days prior to this time. Longshore velocities over the shallow shelf are poleward in both layers. The remnant of the

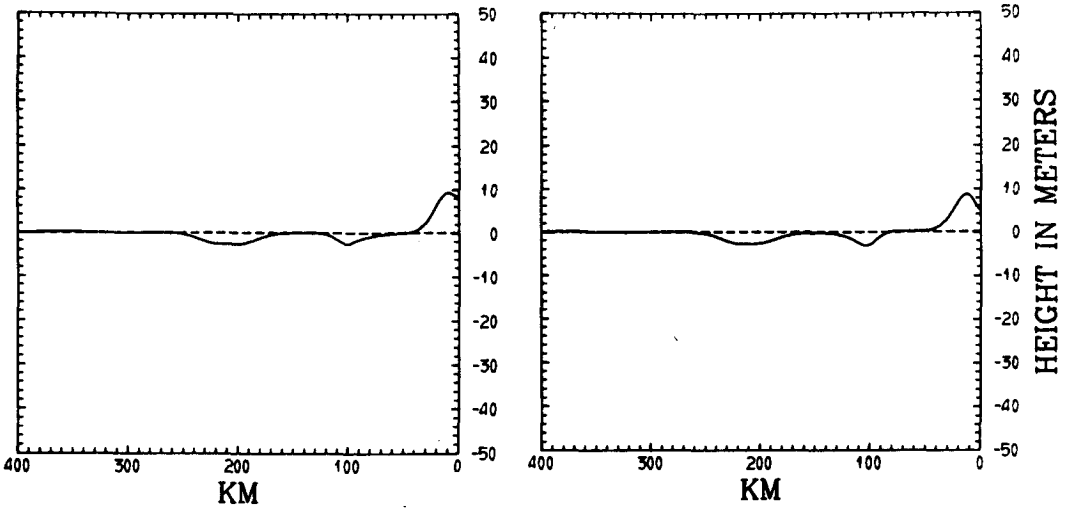

FIG. 11. Height anomalies for the linear (left) and nonlinear (right) models at day 22. Line representations are as in Fig. 7.

equatorward jet in v_1 still remains as a minimum in the poleward flow. Lower layer longshore flow is uniform over the major portion of the shelf.

Decay of the positive height anomaly under strong southerly winds is most rapid at the coastal boundary. Secondary downwelling appears over the continental shelf break. Associated with the lowering of the pycnocline near shore is the development of a sharp, narrow poleward jet within 10 km of the coast in the upper layer. This feature is consistent with the approximate baroclinic velocity relationship of Eq. (23). A similar feature is observed at day 15 in the nonlinear model. Note the difference between the linear and nonlinear models.

b. Time-dependent profiles

Clearly the snapshot approach cannot provide the continuity necessary to develop a comprehensive view of the height and flow fields over time. Fig. 12 shows contours of upper layer longshore flow for the nonlinear model for the first 20 days of integration. Appreciable longshore currents develop in the upper layer after day 9. Outside the forced region the inertial oscillations dominate the flow.

The equatorward jet is depicted by the elongated contours parallel to the coast. The jet becomes well defined at day 13, following the maximum northerly wind at day 12. Note that the axis of the jet moves off shore as time proceeds. If we refer to the contour of pycnocline height anomaly in Fig. 13, we observe that the jet axis follows the position of maximum height gradient. In accordance with the potential vorticity equations (19) and (20), regions where the magnitude of the longshore velocity gradient is large correspond to areas of strongest upwelling or downwelling.

The width of the primary upwelling zone, once established, does not vary appreciably in time. At day 15 the primary upwelling extends to roughly 35 km offshore. Under varying winds from day 15 to day 20 the zone width remains constant. Note that very near the coast the maximum upwelling decreases after day 16.

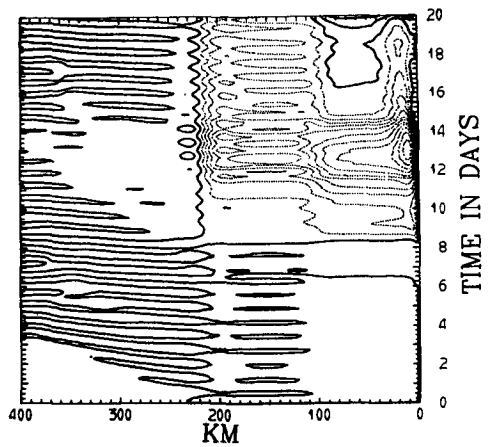

FIG. 12. x-t contours of v_1 for the nonlinear model. Dashed lines indicate negative values and solid lines indicate non-negative values. The contour interval is 2 cm sec^{-1}.

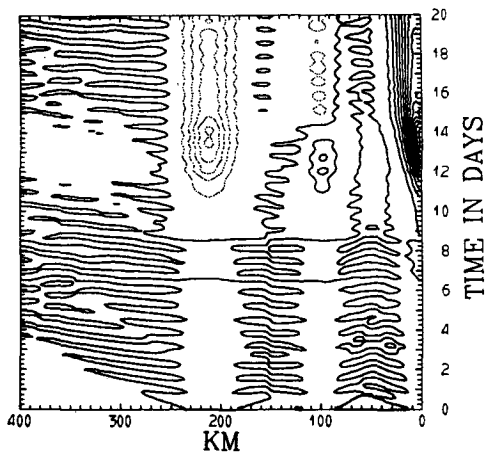

FIG. 13. x-t contours of the interfacial height anomaly for the nonlinear model. Dashed lines indicate negative values and solid lines indicate non-negative values. The contour interval is 2 m.

Our result agrees well with recent observations by Mooers *et al.* (1972) off the Oregon Coast. They found that during the upwelling season the seaward edge of the upwelling zone, as represented by a surface front, remained stationary roughly 30 km off shore. The width of the upwelling zone only varied under a strong seasonal reversal of the winds.

The relationship between the winds, longshore currents, and height anomalies in the jet region 10 km off shore is clarified in the unfiltered time series of Fig. 14. The winds from Fig. 4 have been replotted to facilitate comparison. All data are plotted every 30 min.

During the first five days the winds are highly variable and of low amplitude. During this period there is virtually no upwelling, as indicated by the pycnocline height anomaly time series. Longshore currents are less than 5 cm sec^{-1} during the period. The advent of strong northerlies at day 8 is accompanied by almost immediate barotropic response in the longshore flow. By day 12 the northerly wind brings a sharp increase in the pycnocline height anomaly and the longshore current amplitude. Note the barotropic component is $\sim$20 cm sec^{-1} at day 12.

While the wind speed maximum appears at day 12, the maximum pycnocline height anomaly occurs at day 14. Maximum upper and lower layer longshore currents speeds occurs at day 13, the upper layer maximum lagging the lower layer maximum by some 6 hr. This is in part due to internal waves in the solutions.

Outside the coastal jet region current speeds and pycnocline height anomalies have smaller magnitude. The inertial mode becomes more evident in the time series with distance offshore. In the unforced region the inertial mode is essentially the only remaining feature of the time series.

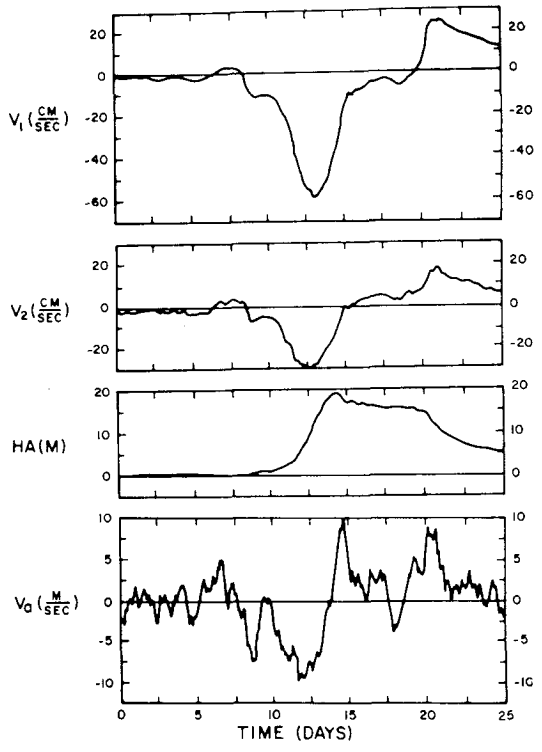

FIG. 14. Time series of winds, currents, and pycnocline height anomalies at 10 km off shore.

c. Spectral studies

Spectral analysis allows efficient presentation of the large amount of data from the model. We have employed it to calculate coherence-squared and phase spectra between the winds and output from the nonlinear model. We have also used current autospectra to compare the linear and nonlinear models and to compare the nonlinear model with actual observations. We find highest coherence at lowest frequencies for the zonal current component vs wind in both layers with a 180° phase shift between the upper and lower layers at frequencies $\lesssim 3$ cpd. Maximum coherence-squared for both the longshore current components vs wind and the pycnocline height anomaly vs wind occurs for winds having a 5-day period. We find minor differences between the linear and nonlinear model current autospectra and major similarities between the nonlinear model and the observed current autospectra.

A more quantitative description of the response of the currents to the winds may be obtained by reverting to coherence-squared and phase spectra for the two components of the currents in each layer vs the wind at 10 km offshore (Fig. 15). Our results may be compared directly with those obtained by Huyer and Pattulo (1972) over the continental shelf off Oregon during summer, 1969.

Fig. 15a depicts coherence-squared and phase between zonal components in each layer and the wind, while Fig. 15b shows the same calculations for the longshore components vs wind. In each case the 95% confidence interval for coherence-squared was 0.53. Thus, at the 95% level, coherence-squared values >0.53 are significantly different from zero. Our coherence-squared values are generally higher than those calculated from actual field data due to the exact nature of our "observed" quantities. The large excursions at frequencies >1 cpd are primarily due to the relatively narrow bandwidth (0.09 cpd) used. However, use of a wider bandwidth does not significantly alter the results we will present here.

The high coherence-squared between zonal components and the wind at frequencies <0.3 cpd is a notable feature of Fig. 15a. This result is absent in the calculations presented by Huyer and Pattulo (1972), most likely due to low signal-to-noise ratio in the observed data. Note that in our calculations there is virtually no difference in coherence-squared values between upper and lower layer components at frequencies below 0.5 cpd.

An even more interesting result is shown in the phase spectra of Fig. 15a. Note that the upper layer zonal flow lags the wind by $\sim 15°$ in the low frequencies below 0.3 cpd and the lower layer zonal component leads the winds by 165° in the same band. The zonal currents are consistently 180° out of phase up to 3 cpd, although caution in phase estimation is warranted when coherence-squared values fall below 0.53. Similar phase spectra are observed over all the forced region of the model. Our result that the inertial oscillations are exactly out of phase in the layers agrees with the findings of Schott (1971) for a highly stratified North Sea.

Phase and coherence-squared spectra for the longshore components of the current in each layer vs the wind are presented in Fig. 15b. The primary result here is that the maximum coherence-squared value for both components appears at 0.2 cpd, corresponding to a period of 5 days. This peak is also observed in the coherency-squared spectrum of winds vs pycnocline height anomalies, as might be expected. At 0.2 cpd the current lags the wind by about 60°; at lower frequencies the lag is 10°–20° less.

As noted earlier, the upper and lower layer longshore flow contains a strong barotropic component. This fact is emphasized in the low-frequency phase spectra of Fig. 15b. Below 1 cpd the phase difference between upper and lower layer longshore components never exceeds 10° and is considerably less at most frequencies. Above 1 cpd the phase difference increases and is especially large and erratic above the inertial frequency. Note that above 1 cpd the coherence-squared for the upper layer longshore component is generally higher than its lower layer counterpart.

We have not attempted to offer explanations for each peak in the coherence-squared spectra of u and v above 1 cpd. Many of these peaks are due to wave reflections in the model and may be removed by appropriate

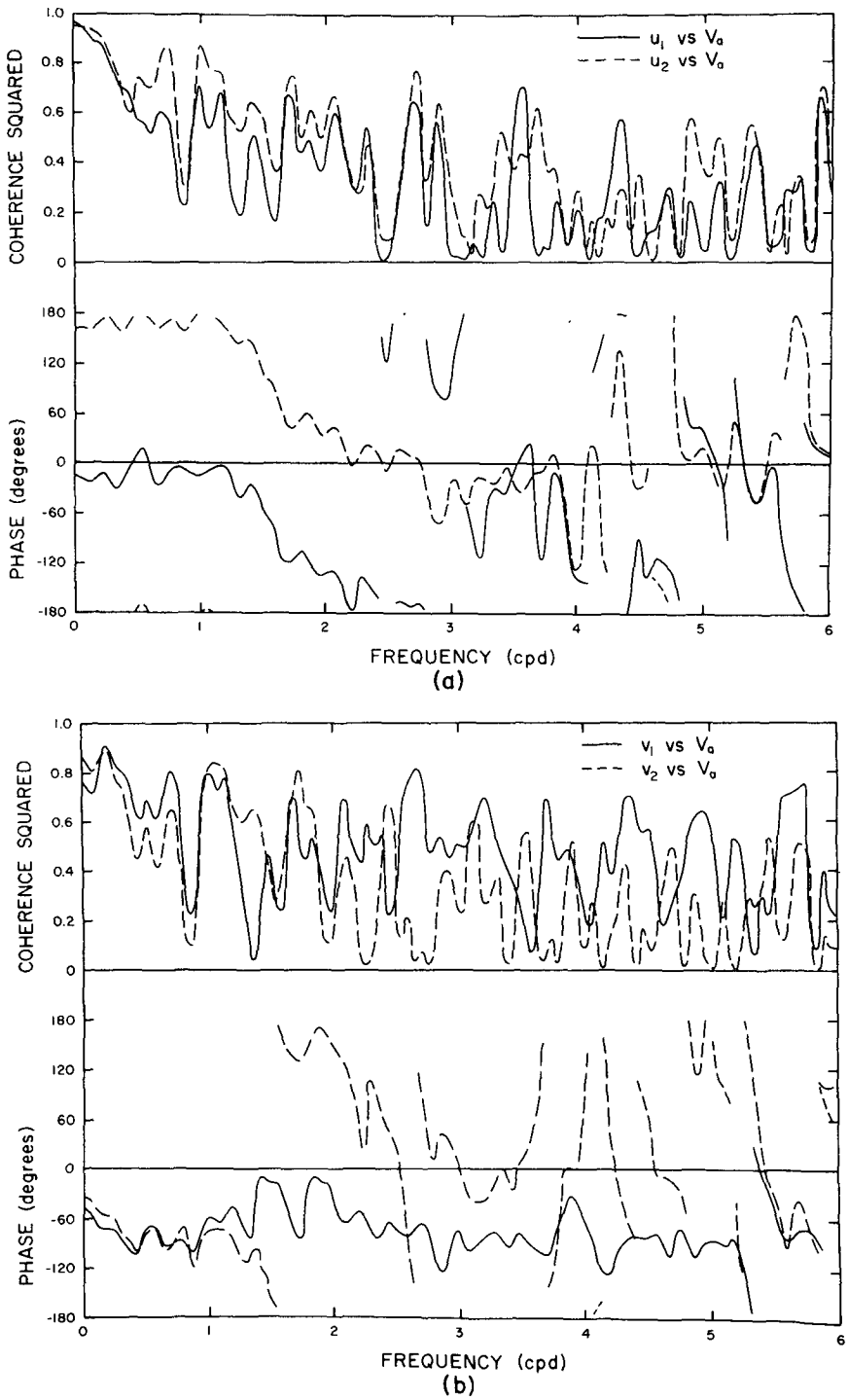

FIG. 15. Coherence-squared and phase spectra for (a) winds vs upper and lower layer zonal current components and (b) winds vs upper and lower layer meridional components 10 km off shore.

filtering. A wider bandwidth would also contribute to removing several smaller peaks. We do point out, however, that although there are no sea breeze effects represented in our kinetic energy spectrum of wind speed nor are tidal motions accounted for, in the model equations, a significant coherence-squared value at about 1 cpd is noted for both longshore components vs wind and in the lower layer zonal component vs wind. These peaks have not been satisfactorily explained.

Fig. 16 shows the current autospectra for longshore and onshore components from both the nonlinear model

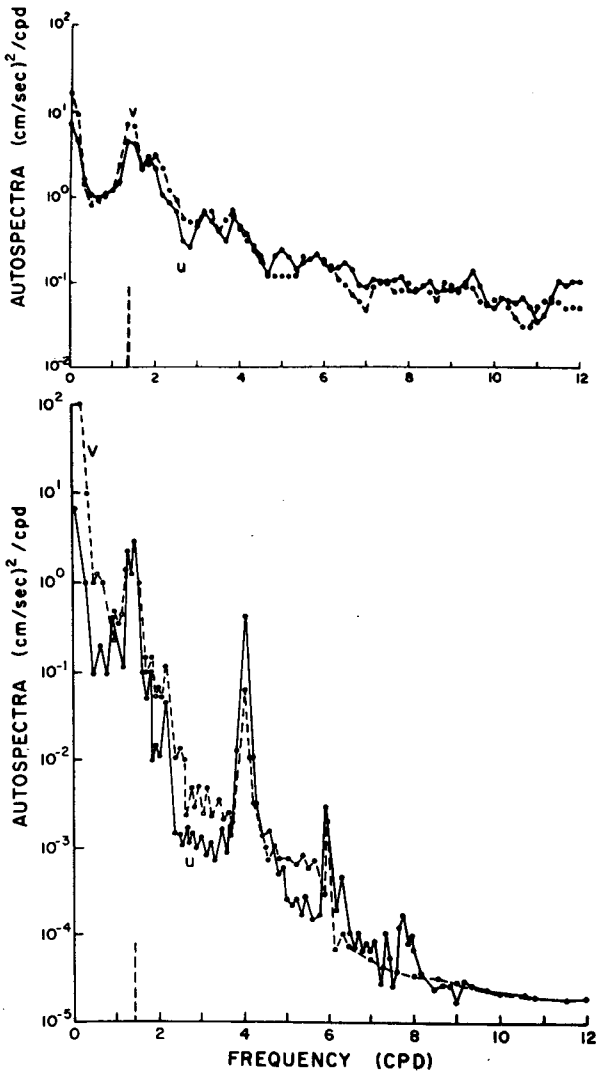

FIG. 16. Observed current autospectra (top) due to Mooers (1970) and current autospectra from the nonlinear model (bottom) vs frequency (cpd).

and the observed data. The model data are taken from the lower layer, 100 km offshore on the sloping shelf. Total water depth is 125 m. Model data were obtained every 30 min for the entire 25-day period. Thus, the fundamental frequency is 0.04 cpd and the Nyquist frequency is 24 cpd. Since little energy exists in frequencies >12 cpd, only the range of frequencies 0–12 cpd is plotted. Prior to spectral estimation the data were detrended and the mean removed. Raw spectral estimates were smoothed by a single Hanning operation.

The observed autospectra were obtained by Mooers (1970) at the seaward edge of the continental shelf off the coast of Oregon from 8 August to 9 September, 1966. Total ocean depth was 200 m and the current meter was at 60 m, situated below the seasonal thermocline. Sampling was at hourly intervals. The mean and linear trend were moved and spectral estimates were smoothed using the Hanning procedure. The 90% confidence interval is half the width of one decade on the ordinate.

The maxima of both the observed and model autospectra occur at the low-frequency limit. Here the spectral level for the longshore current in the model is larger than the observed. The onshore spectral level for the model agrees well with the observed value.

The spectral level decays rapidly for frequencies below the inertial frequency. In the observed case the inertial period is 16.9 hr and in the model the value is 17.4 hr. Peak amplitude of the inertial oscillations for the model is ~ 3 (cm sec^{-1})^2 cpd^{-1} for both components of current velocity. In the observed case the longshore peak is 7 (cm sec^{-1})^2 cpd^{-1} and the onshore peak 5 (cm sec^{-1})^2 cpd^{-1}. In both cases the inertial energy spreads over the frequency band of width 0.2 cpd, giving a double-peak structure to the representations.

Although the spectral levels range over many orders of magnitude, the model and the observed autospectra at the inertial frequency differ by a small amount. This is a remarkable result. It is certainly unexpected since the model may be regarded as a crude approximation of nature at best.

For frequencies greater than the inertial, spectral values decrease rapidly. This decrease is more marked in the model autospectra. Aliasing from frequencies >12 cpd may account for the consistently higher spectral levels found between 2 and 12 cpd in the observed autospectra. At frequencies >8 cpd both autospectra tend to approach a -2 slope as plotted on a log-log scale.

Peaks at 4, 6 and 7.7 cpd in the model autospectra are due to barotropic surface gravity waves. These waves reflect between the far wall and the coastal boundary with angular frequency dependent on wavelength and water depth. A kinetic energy spectral representation indicates these waves comprise less than 1% of the total kinetic energy of the system. Therefore, they are unimportant to the macroscopic nearshore currents with which we are concerned. Because these waves reflect in the east-west direction, the u_2 autospectra show the largest wave amplitude at the reflection frequencies. The v_2 autospectra exhibit smaller peaks due to the weak dynamic coupling between u_2 and v_2. Use of the open ocean boundary conditions may remove these waves (Wurtele *et al.*, 1971).

Fig. 17 compares the u_2 current autospectra for the linear and nonlinear models at 50 km offshore. Spectral estimates were obtained as described above, using an hourly sampling interval.

The maximum energy is found at the low-frequency limit of the frequency range. It is more than 10 times larger than that calculated for u_2 at 100 km in the nonlinear case. The increase is due to decreased thickness of the lower layer inshore of the shelf break.

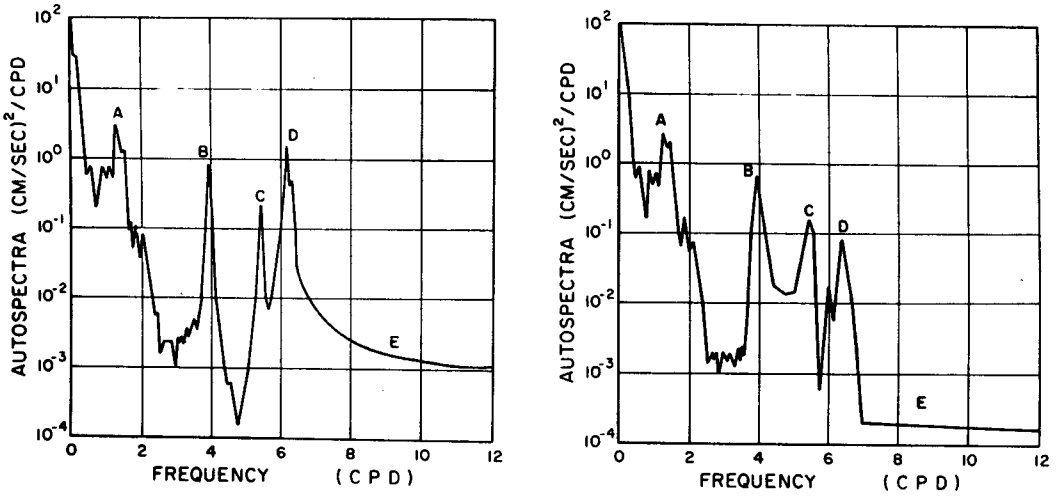

FIG. 17. Current autospectra of u_2 for the linear (left) and nonlinear (right) models at 50 km off shore.

Spectral levels decrease rapidly with frequency in the two models. A discrepancy appears in the inertial band near 1.33 cpd (peak A). The nonlinear inertial band contains a two-peak structure with nearly identical values for each peak. In the linear model the higher frequency peak is negligible. Note that the numerical model is deterministic and results reproducible. For a given set of initial conditions and model forcing, even small differences between models can be considered real. Thus, we attach significance to the above discrepancy and attribute the fine structure in the inertial maximum to nonlinear effects.

Above the inertial frequency, up to 4 cpd, both autospectra behave similarly. At 4 cpd the surface gravity wave peak is observed in both models, covering a broader frequency range in the nonlinear case. Spectral broadening is a general feature of the nonlinear model autospectra.

The total kinetic energy within a band $\Delta f=0.2$ cpd centered at 4 cpd is larger in the nonlinear model. Further, the spectral gap appearing near 5 cpd in the linear case is substantially filled in the nonlinear autospectrum. With the linear results as reference, we observe other changes in the nonlinear u_2 autospectrum: first, peak C exhibits spectral broadening and a slight decrease in the value of the relative maximum; second, a smaller relative minimum is noted just below 6 cpd and between 6 and 7 cpd the spectral level is consistently lower; third, the relative maximum at peak D appears at higher frequency; and finally, lowering of the spectral level is observed for frequencies >7 cpd.

In summary, at frequencies <4 cpd only slight differences appear in the u_2 autospectra for the linear and nonlinear cases. The most significant difference appears at the high-frequency end of the inertial band. Between 4 and 5.5 cpd the spectral level is larger in the nonlinear model than in the linear case. Above 5.5 cpd the reverse is observed, with largest differences appearing above 7 cpd. It appears that high-frequency wave energy is transferred to intermediate frequencies in the u_2 nonlinear model. Similar energy transfers in u_1, v_1, and v_2 have been noted in some (but not all) autospectra taken at varying distances off shore. Longshore components indicate weaker transfers than their cross-stream counterparts. It is conjectured that since the longshore balance is geostrophic this energy is not as available for scale interchange.

There is observational evidence that high-frequency oscillations of winds and waves can contribute to wave energy at intermediate frequencies (Huyer, 1971). In our model, however, their importance to the macroscopic dynamics of coastal upwelling is minor. Only a small fraction of the total kinetic energy of the system resides in those frequency bands where transfers occur.

Internal waves are known to occur in the model also. They appear in contour plots of pycnocline vertical velocity and are seen in the tilting contours in the lower left corner of Fig. 12. Due to their small amplitude they are not important in our solutions. In the real ocean, however, they may be important, as noted by Mooers (1970). Tidal motions, for example, may generate internal waves with significant amplitude.

5. Critique

We have described an extremely simple model of coastal upwelling. Thermodynamic effects, mixing, and all longshore variations have been neglected. Our wind stress forcing is at best a first approximation to the actual conditions in an upwelling situation. Because surfacing of the interface is not allowed, we are limited to studying only the onset of upwelling.

Nevertheless, our results are encouraging. The upper layer longshore coastal jet, the rate of interfacial rise, the character of the current spectra, and the width of the primary upwelling zone are compatible with observations. Notably absent from our model is a deep

poleward countercurrent during active upwelling. O'Brien and Hurlburt (1972) demonstrate that such a feature is not dynamically possible in the present model. [See Hurlburt and Thompson (1973) for a complete discussion of the coastal upwelling undercurrent.]

Clearly, three-dimensional models of coastal upwelling are needed to describe upwelling dynamics. Yet, for these models to be useful, they must be verified by an integrated set of atmospheric and oceanic observations. Large field experiments such as the NSF–IDOE[2] Coastal Upwelling Experiment (CUE) are planned for the major upwelling regions. They may provide the first detailed picture of the time and space distribution of meteorological and oceanographical variables in an active upwelling zone needed to test the present and more complicated numerical models.

6. Summary

The response of a linear and a nonlinear two-layer numerical model of coastal upwelling on an f-plane has been examined under time-dependent forcing. A technique is described whereby time-dependent winds are generated from a kinetic energy spectrum of wind speeds.

Coherence-squared spectra for the winds vs zonal current components in the upwelling zone indicate highest coherence at lowest frequencies. A 180° phase shift is observed between upper and lower layer zonal currents at frequencies <3 cpd. Coherence-squared spectra for longshore currents vs winds and pycnocline height anomalies vs winds exhibit a maximum value at a frequency corresponding to a 5-day period.

Comparisons between the linear and nonlinear models indicate that the essential features of coastal upwelling can be described using linear dynamics. However, results from the nonlinear model are compatible with certain observed features from the real ocean. In particular, current autospectra from the nonlinear model agree remarkably well with observed autospectra at frequencies below the inertial.

Acknowledgments. This paper is the basis for a Master's thesis for Mr. Thompson in the Department of Meteorology of Florida State University. Mr. Thompson has been supported in part by a UCAR fellowship. J. J. O'Brien has been supported by NCAR during the summers of 1970 and 1971. Primary research support was supplied by the Office of Naval Research. Partial support was obtained from the National Science Foundation under Grant GA-29734. The Computer Facility at NCAR provided CDC 7600 and 6600 time and the Florida State University Computing Center provided CDC 6400 time.

Our appreciation is extended to Dr. Christopher Mooers, Dr. Ya Hsueh, Harley Hurlburt, and John Lee for their stimulating comments and suggestions during the course of this research.

[2] International Decade of Ocean Exploration.

REFERENCES

Bang, N. D., 1971: The southern Benguela Current region in February, 1966: Part II. Bathythermography and air-sea interactions. *Deep Sea Res.*, **18**, 204–224.

Bye, J. A. T., 1970: Eddy friction in the ocean. *J. Marines Res.*, **28**, 124–134.

Charney, J. G., 1955: The generation of oceanic currents by wind. *J. Marine Res.*, **14**, 477–498.

Ekman, V. W., 1905: On the influence of the earth's rotation on ocean currents. *Ark. Mat. Astron. Fysik.*, **12**, 1–52.

Grammeltvedt, A., 1969: A survey of finite-difference schemes for the primitive equations of a barotropic fluid. *Mon. Wea. Rev.*, **97**, 384–404.

Hidaka, K., 1954: A contribution to the theory of upwelling and coastal currents. *Trans. Amer. Geophys. Union*, **35**, 431–444.

Hino, M., and K. Hino, 1965: Response characteristics of Tokyo Bay to incident long waves. *Coastal Eng. Japan*, **8**, 57–69.

Hsueh, Y., and R. N. Kenney III, 1972: Steady coastal upwelling in a continuously stratified ocean. *J. Phys. Oceanogr.*, **2**, 27–33.

——, and J. J. O'Brien, 1971: Steady coastal upwelling induced by an along-shore current. *J. Phys. Oceanogr.*, **1**, 180–186.

Hurlburt, H. E., and J. D. Thompson, 1973: Coastal upwelling on a β-plane. *J. Phys. Oceanogr.*, **3**, 16–32.

Huyer, A., 1971: A study of the relationship between local winds and currents over the continental shelf off Oregon. Master's thesis, Oregon State University, Corvallis.

——, and J. G. Pattulo, 1972: A comparison between wind and current observations over the continental shelf off Oregon, summer 1969. *J. Geophys. Res.*, **77**, 3215–3220.

Johnson, J. A., 1970: Oceanic boundary layers. *Deep-Sea Res.*, **17**, 455–465.

Kullenberg, G., 1971: Vertical diffusion in shallow waters. *Tellus*, **23**, 129–135.

Kwizak, M., and A. Robert, 1971: A semi-implicit scheme for grid point atmospheric models of the primitive equations. *Mon. Wea. Rev.*, **99**, 32–36.

Millard, R. C., 1971: Wind measurements from buoys: A sampling scheme. *J. Geophys. Res.*, **76**, 5819–5828.

Mooers, C. N. K., 1970: The interaction of an internal tide with the frontal zone in a coastal upwelling region. Ph.D. dissertation, Oregon State University, Corvallis.

——, C. A. Collins and R. L. Smith, 1972: The dynamic structure of the frontal zone in the coastal upwelling region off Oregon. (Submitted to *J. Phys. Oceanogr.*)

O'Brien, J. J., and H. E. Hurlburt, 1972: A numerical model of coastal upwelling. *J. Phys. Oceanogr.*, **2**, 14–26.

Pike, A. C., 1971: Intertropical convergence zone studied with an interacting atmosphere and ocean model. *Mon. Wea. Rev.*, **99**, 469–477.

Pillsbury, D., 1972: A description of hydrography, winds and currents during the upwelling season near Newport, Oregon. Ph.D. dissertation, Oregon State University, Corvallis.

Proudman, J., 1953: *Dynamical Oceanography*. Methuen, London, 409 pp.

Schott, F., 1971: Spatial structure of inertial-period motions in a two-layered sea, based on observations. *J. Marine Res.*, **29**, 85–102.

Sielecki, A., and M. G. Wurtele, 1970: The numerical integration of the non-linear shallow-water equations with sloping boundaries. *J. Compul. Phys.*, **6**, 219–236.

Smith, R. L., 1968: Upwelling. *Oceanography and Marine Biology, Annual Review*, H. Barnes, Ed., London, Allen and Unwin, 11–47.

Wurtele, M. G., J. Peagle and A. Sielecki, 1971: The use of open ocean boundary conditions with the storm-surge equations. *Mon. Wea. Rev.*, **99**, 537–544.

Yoshida, K, 1967: Circulation in the eastern tropical oceans with special reference to upwelling and undercurrents. *Japan. J. Geophys.*, **4**, 1–75.